



Outdoor thermal comfort in urban neighbourhoods by coupling of building energy simulation and computational fluid dynamics

Marzieh Fallahpour^a, Reihaneh Aghamolaei^b, Ruijun Zhang^c, Parham A. Mirzaei^{c,*}

^a College of Fine Arts, Department of Architecture and Energy, University of Tehran, Tehran, Iran

^b School of Mechanical and Manufacturing Engineering, Faculty of Engineering and Computing, Dublin City University, Whitehall, Dublin 9, Ireland

^c Architecture and Built Environment Department, University of Nottingham, University Park, Nottingham, NG7 2RD, UK



ARTICLE INFO

Keywords:

Outdoor thermal comfort
Computational fluid dynamics
Building energy simulation
Tempo-spatial
Convective heat transfer coefficient
Solar radiation

ABSTRACT

When evaluating the outdoor environment, it is essential to improve the accuracy of outdoor thermal comfort (OTC) modelling by investigating the simultaneous interactions of both convective and radiative fluxes. The majority of the existing models, however, employed to evaluate thermal comfort, do not consider these co-effects.

This study aims to develop a novel and comprehensive framework for OTC modelling while using non-isothermal airflow and surface temperatures within street canyons. For this purpose, a dynamically coupled building energy simulation (BES) and computational fluid dynamics (CFD) model, previously developed by authors, is used to provide detailed analysis of convective fluxes. These values in addition to the simulated radiative heat fluxes are then utilized to calculate the OTC at a neighbourhood case study during a typical hot day.

The results show substantial changes (6.5% higher) in the OTC results using the newly developed coupled model in comparison to traditional (standalone) approaches. For example, in the coupled approach, the OTC values experience a wider range which peaks to at noon. Moreover, physiological equivalent temperature (PET) values are higher which shows higher level of discomfort and heat stress range compared to the standalone models.

1. Introduction

Outdoor thermal comfort (OTC) has been turned into a pivoting parameter in urban planning with respect to outdoor activities, social connections, tourism, wellbeing, and health in recent years [1–3]. Extreme heat has been experienced in urban areas as a result of global climate change and growing urbanisation in the past decades [4]. Aside from local climate conditions, key elements determining OTC are urban geometry [5], thermal qualities of urban surfaces [6], and urban landscaping [4,7]. The retention of solar heat in building materials and ground surfaces, as well as the blocking and reabsorption of night-time outgoing longwave radiation by sky-obscuring structures, all contribute to the formation of urban heat island (UHI) phenomena [4,8]. Poor OTC conditions have been widely addressed as a severe side effect of the UHI [4].

It is critical to precisely analyse and comprehend the spatial and temporal variations in OTC to be able to appropriately countermeasure

the consequences of UHI, in addition, to transform urban sidewalks into comfortable spaces. As the result, planners need to be equipped with tools to analyse cities' physical environment to identify and to mitigate the effects of changing micro-thermal conditions [7,9]. This implies that identification and analysis of pedestrian thermal comfort levels in street canyons can lead to determination and investigations of the outdoor thermal condition of metropolitan environments to develop heat stress-reducing strategies [2,9–11].

In this regard, simulation-driven microclimate analysis methodologies are widely implemented in the early design phases to achieve a maximum impact on microclimates [11–13]. Computational models for analysing outdoor thermal comfort are straightforward in the implementation process and also less expensive compared to full-field measurements campaigns, particularly when a full investigation of vast urban regions is desired [12,13]. Computational models are, however, constrained by the deficiency of simulation and numerical techniques when taking into consideration the complexities and dynamic nature of urban morphologies [14]. From a heat transfer perspective, both

* Corresponding author. Department of Architecture and Built Environment, University of Nottingham, University Park, Nottingham, NG7 2RD, UK.
E-mail address: Parham.Mirzaei_ahranjani@Nottingham.ac.uk (P.A. Mirzaei).

Nomenclature		
Parameter unit Explanation		
U	m/s	flow velocity
z	m	altitude, height from ground
δ	m	site boundary layer thickness
k	J/kg	turbulence kinetic energy
ε	m^2/s^3	turbulent dissipation rate
I	–	turbulence intensity
a	–	exponent of wind speed profile
u_z'	m/s	rms velocity fluctuation
C_μ	–	$k - \varepsilon$ model constant
L_a	k/m	air temperature gradient within troposphere
E_r	m	radius of the Earth
T_a	°C	air temperature
T_b	°C	air temperature at ground level
T_s	°C	building surface temperature
h_c	W/m^2K	convective heat transfer coefficient
h^*	W/m^2K	virtual h_c for EnergyPlus
q''_c	W/m^2	convective heat flux
k_s	m	roughness height
C_s	–	roughness constant
z_0	–	aerodynamic roughness length
TCP_w	–	weighted Temporal Comfort Performance
TC_{ij}	–	timely average of the thermal comfort score
C_{min}, C_{max}	°C	maximum and minimum thresholds of acceptable comfort range
ΔT_{comf}	°C	amplitude of the acceptable comfort range
T_{ij}	°C	local thermal comfort value at each point

radiative and convective fluxes are key contributors to the OTC assessment in outdoor spaces, which add to the complexity of OTC and numerical simulations in comparison to indoor spaces, especially in densely populated microclimates where the influence of the surrounding neighbourhood is significant [15,16]. Nonetheless, for accurate OTC calculations, the interactions and effects of the building shells or external surfaces, which depend on the indoor energy consumption and the heat transfer between a building envelope and its surrounding microclimate, should be considered [16–18].

To this end, a wide range of building energy simulation (BES) tools such as EnergyPlus, REVIT, DOE-2, and REQUEST are utilized to calculate heating and cooling loads by using numerous empirical and semi-empirical convective heat transfer coefficients (CHTC) correlations on the external surfaces [19–21]. However, these correlations are mainly developed for isolated building scenarios and incapable in capturing of the impact of local dynamic airflows. On the other words, these correlations employ simplified exterior airflow models that ignore the neighbourhood effect to determine the external surface temperature of buildings, which result in significant inaccuracies in the calculation of convective heat transfer. Due to this issue, forecasting a total building energy demand has been observed to have at least about 20–40% errors in the calculations [22]. On the other hand, the widely used models to investigate OTC are based on the comprehensive analysis of radiative fluxes, such as ENVI-met, SOLWEIG, RayMan, SkyHelios, Ladybug-Grasshopper plugins [11,23–25]. These tools are capable of performing OTC analysis with high-resolution tempo-spatial results [26, 27], addressing the distribution of OTC in outdoor environments. However, reviewing the related literature shows that a major limitation of OTC tools is associated to their incapability to obtain buildings' external surface temperatures interlinked with dynamic thermal response of buildings [28]. Inversely, the simplified temperature of buildings' external surface is employed without considering co-effects of the buildings' dynamic thermal response and airflow, or the wind velocity is mainly found from predefined static values from weather data files. For example, Evola et al. [11] implemented a workflow in the Grasshopper platform to calculate OTC by taking into account the interaction of the building envelope with both indoor and outdoor areas, however, the effect of the dynamic airflow was ignored, and the static value of wind velocity from the weather data files was used. One solution to such limitation is to integrate microclimate CFD models to include the dynamic impact of wind velocity resulting from neighbourhood effects, especially in complex urban cases. CFD microclimate models are widely used to solve conservation laws at several scales, and to assess pedestrian thermal comfort in urban areas [29]. CFD has been used in a wide range of environmental investigations, from indoor environments to neighbourhood and urban communities [16,30–39]. However, in addition to validation concerns and domain size constraints

(a few hundred meters), calculating radiative fluxes is computationally intensive, making microclimate CFD models less common in OTC investigations [29,40].

Microclimate CFD models are mainly concerned with the isothermal solution of convective fluxes. Nonetheless, consideration of non-isothermal solutions can potentially account for considerably more accurate results in the OTC calculations as convective heat transfer has two to three times higher impact on the heat flow over building facades than radiative heat transfer [41–43]. As a potential limitation of CFD microclimate models, they do not account for the effect of a building's dynamic response on microclimatic calculations, which negatively impacts on the OTC evaluations [15]. For example, Nazarian et al. [44] improved the methodology of outdoor thermal comfort prediction using CFD simulations and the index Standard Effective Temperature (SET), which led to the improvement of the thermal comfort calculation. However, the dynamic impact of the buildings and latent heat flux were neglected.

As a potential solution to overlap the limitations of each modelling approaches, BES and CFD tools can be coupled together to benefit from each other strength to assess buildings' energy demand with a good representation of convection fluxes on their external surfaces [45]. For example, to investigate the local urban microclimate's impact on the building energy demand, the method of coupling CFD and BES models was performed in several studies [46,47] for assessing the building's energy demand. This method can result in improving building performance and eventually better urban environmental designs.

Furthermore, the coupling CFD-BES approach has been conducted to analyse the short-term to long-term effects of both naturally and mechanically ventilations in communities [18]. In this regard, the CFD domain has the capacity to generate a more realistic convection coefficient to be fed to the BES tools, and inversely, the BES domain enables the microclimate CFD model to account for the building's dynamic thermal response. This implies that the convective heat transfer coefficient and surface temperature data are shared between the CFD and BES tools. For example, to investigate the environmental factors that affect the OTC performance, Zhang et al. [15] used modelling of solar radiation, heat storage, and CFD to obtain an improved prediction of CHTC values, and subsequently, the improved evaluation of energy demand of buildings located in urban neighbourhoods. Zhang et al. [18], also, introduced a pioneering integrated CFD-BES-artificial intelligence framework for evaluating CHTC profiles, which is significantly quicker than the existing techniques. Despite the coupling approaches' ability to provide building surface temperatures, this method is rarely used for the OTC assessments. Aghamolaei et al. [16] proposed a novel simulation framework for outdoor environments to couple the radiation and convection fluxes as OTC values changed notably along the building's perimeters and edges, where considerable velocity gradients have been

detected. However, the dynamic effect of the external surface temperature distribution on the airflow was neglected. To this end, a review of previous literature indicates the importance and necessity of using a comprehensive method for the OTC assessment that simultaneously considers all the influential factors of the tempo-spatial distribution of OTC, including radiative and convective fluxes. This demands concurrent calculations of energy demand and surface heat transfer exchanges of buildings.

Hence, this study aims to develop a novel framework to improve the OTC analyses. For this purpose, this framework couples a validated CFD model as a powerful tool for the convective fluxes calculation and a BES model for considering the buildings' energy demand and consequently their surfaces' dynamic thermal response. This paper thus uses the results of authors' previous study [15], which includes the external surface temperature of buildings from a BES and CFD coupling approach, and the proposed method by another study of authors [16], which contains a coupling of CFD and radiation-based modelling for the OTC analyses. The proposed framework in this study provides a computationally efficient method with a high-resolution, which is implemented in Grasshopper platform and is evaluated against a benchmark model of a simplified neighbourhood located in Los Angeles during the summer.

In this paper, the tempo-spatial OTC modelling framework is discussed in Section 2, which outlines a process for developing the OTC model of the selected neighbourhoods. The results of the applied methodology for analysing the comfort performance of the specified scenarios are presented in Section 3 followed by further discussions. Finally, Section 4 provides the conclusions as well as additional study recommendations.

2. Methodology

In this study, a sequential procedure was implemented to develop an improved OTC modelling framework in the complex urban settings as shown in Fig. 1. This framework includes four steps. (1) At Step-1, a dynamic coupled BES-CFD model is employed to calculate the hourly building surface temperature. These results are then used in the CFD simulations for more accurate hourly air velocity calculations; (2) This step includes the effects of different external surface temperatures obtained from Step-1 on the air velocity close to the buildings approaching from different directions; (3) In Step-3, the radiative fluxes between buildings' exterior surfaces are calculated based on the results obtained from two previous steps; (4) Finally, the results of all steps are implemented in an embedded comfort model, investigating the OTC of the building neighbourhood at Step-4.

2.1. Case definition

Nine cuboid commercial structures ($L = W = H = 10$ m) arranged in a 3×3 grid were built for representing a small urban neighbourhood as shown in Fig. 2. The width of all the streets was 10 m, as a result, the aspect ratio of each street canyon was unity and the same. The central building model as the target building for the BES-CFD coupling method had three storeys with floor heights of 3.4 m, 3.3 m, and 3.3 m, respectively, ascending from the ground to the roof. To assist the cross-ventilation flow, windows were placed on the south and north façades of each storey while the window-to-wall ratio was 24.4% for the building's south façade and 19.8% for the other walls. The windows were placed 0.9 m above the ground and covered up to 39.7% of the wall area in the horizontal dimension and 50% in the vertical one. The surrounding buildings were simplified to consist of only one thermal zone with

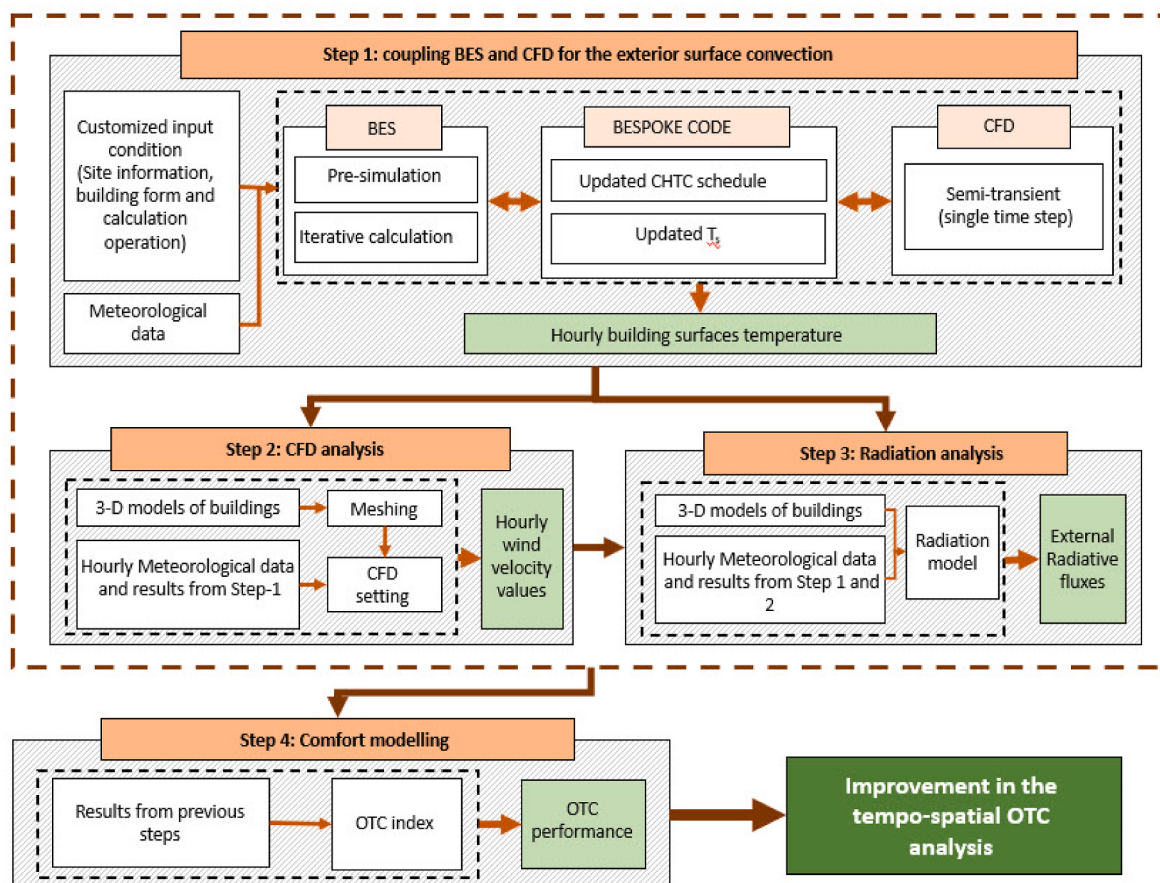


Fig. 1. The framework of the novel OTC modelling framework.

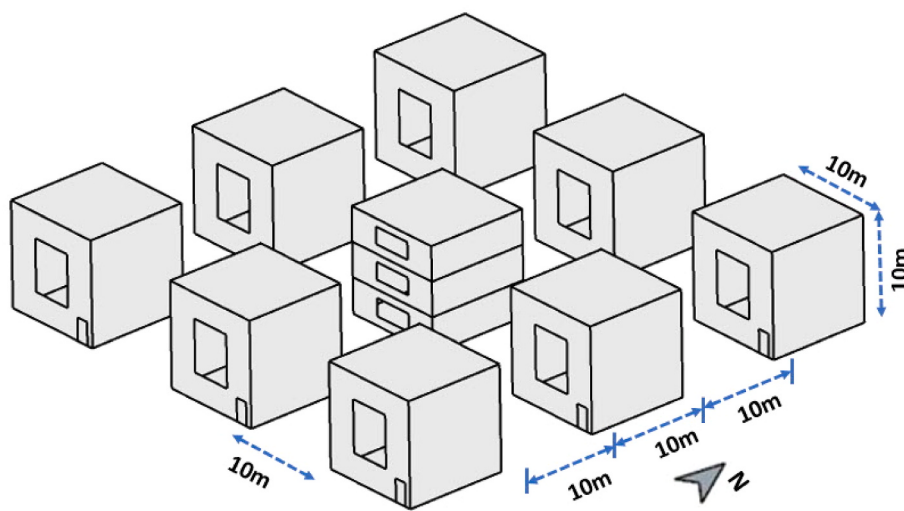


Fig. 2. Illustration of the idealized neighbourhood as the case study.

windows placed 2.45 m above the ground while the window-to-wall ratio was maintained the same similar to the central building as displayed in Fig. 2. Every building model featured an entrance door with a height of 2.13 m and a width of 1 m on the south façade.

Simulations were conducted in the explained idealized case study neighbourhood located on the city of Los Angeles on 25th of September, representing the warmest workday of the year in this city. The temperature fluctuated from 18.1 °C to 34.1 °C on a daily basis. After sunset at 6 p.m., there was no sunlight until daybreak on the following morning. The predominant wind direction was 50° (clockwise from North) at 3.1 m/s, according to the local meteorological data. Except for the national holidays, the target building was occupied between 7 a.m. and 9 p.m. on weekdays with an operative temperature maintained at 21.0 °C–24.0 °C for the occupying hours. During the rest hours, the zones were controlled between 15.6 °C and 26.7 °C. The occupancy reached up to 95% by 9 a.m. and then decreased to 50% between 12 and 1 p.m. for the lunch break. Only 30% of the target building's occupants remained at 5 p.m. and then after the presence dropped to 10% by 7 p.m. The other settings of the case study for the building energy simulation are presented in Table 1.

The idealized case study neighbourhood is similar to the Architectural Institute of Japan (AIJ) Case C geometric model [48,49], which facilitates the required experimental data to validate the CFD model. Also, the features of windows, walls, and operational conditions within these arrangements were referred to a benchmark model of small office concept suggested by U.S. Department of Energy (DoE) [50]. Because this framework represents the spatial and temporal alteration of OTC in a metropolitan environment, the simulations were run over the duration of a whole day (7:00–18:00 on 25th September). Furthermore, Table 2 presents the corresponding solar radiation, wind velocities, and directions from the climatic data of Los Angeles utilized for the CFD simulations as the input parameters.

Table 1

Input parameters as location and building characteristics for building energy and CFD simulations.

Input parameters	Inputs
Location	Los Angeles
Latitude and longitude	34.0522° N, 118.2437° W
Heating set point at buildings	21 °C
Cooling set points at buildings	28 °C
U-values of glazing	2.96 W/m ² K
Exterior walls U-value	1.29 W/m ² K
Roof U-value	0.47 W/m ² K

Table 2

The climatic data of Los Angeles at the simulation day (25th September) [51].

Time	Wind velocity (m/s)	Wind direction (°)	Direct solar radiation (W/m ²)
07:00	1.5	140	269
08:00	2.1	10	582
09:00	2.1	350	726
10:00	4.1	230	738
11:00	4.1	260	827
12:00	4.6	270	844
13:00	5.2	260	841
14:00	5.7	230	808
15:00	5.7	240	742
16:00	5.7	240	642
17:00	4.6	250	442
18:00	3.1	230	69

2.2. CFD and BES coupling

For the BES and CFD integration, the external method of coupling was performed while a dynamic technique was employed to verify the convergence for each time-step as described in details in a study by authors [15]. In this study, with developing a bespoke code, the meteorological data and inputs were transmitted between the BES and CFD models. The BES and CFD transferred the results to the bespoke code, which it then generated the input files in a standard format for the BES in addition to some files with commands to automatically setup the boundary conditions in the CFD model. In the pre-simulation of the convective heat transfer calculations, the BES utilized DOE-2 model defined within EnergyPlus. The calculation method of the exterior CHTCs was then switched to 'schedule' with edited schedules of default CHTC values for all surfaces added to the BES input file to start the dynamic simulation.

The transferred variables between the two domains were the building surface temperatures (T_s) of the building energy model and the convective heat transfer coefficients (h_c) of the CFD model. Here, T_s was forwarded to the CFD model to define its boundary conditions while the CFD then returned h_c to the BES. The convergence was achieved for each time-step of the simulation period. In this regard, three orders of magnitudes for T_s and h_c were determined as the convergence criterion of the coupling process for each time-step. If the iterations number for a single time-step overpassed 20, the convergence criterion was adjusted to two orders of magnitudes, which is considered as an acceptable criterion in terms of prediction accuracy and computational time and cost. The

meteorological data were sent to the BES tool directly while the data were transferred as the imported profiles into the CFD tool, ensuring that the same vertical wind profiles would be captured in both domains.

In this process, EnergyPlus 8.7© was utilized as the building energy tool, ANSYS Fluent 17.2© was used as the CFD simulation tool, and Matlab R2017a© was used to develop the bespoke code.

2.2.1. BES and CFD solver communication

During the coupling stage, all the CFD simulations were run semi-transiently, so that the boundary conditions of the CFD model are updated according to the information from the BES simulation, which would only provide the surface temperature and weather condition for a certain period of time. Within such period of time, the boundary conditions would be considered as steady. The weather data were drawn from the BES domain with the vertical profiles constructed from the local wind velocity U_z (m/s) and air temperature $T_{a,z}$ (°C) at the height z (m) presented by the following equations [49]:

$$U_z = U_{met} \left(\frac{\delta_{met}}{z_{met}} \right)^{\alpha_{met}} \left(\frac{z}{\delta} \right)^\alpha \quad (1)$$

$$T_{a,z} = T_{a,z\ met} - L_a \left(\frac{E_r z_{met}}{(E_r + z_{met})} - \frac{E_r z}{(E_r + z)} \right) \quad (2)$$

where α is an exponent and δ (m) is the boundary layer thickness, depending on the terrain type of the selected site. The data obtained at the meteorological station are indicated by the subscript 'met'. 10 m, 270 m, and 0.14 are the default values for z_{met} , δ_{met} , and α_{met} , respectively. $L_a = -0.0065$ K/m is the tropospheric air temperature gradient and $E_r = 6.356 \times 10^6$ m is the Earth's radius. The local turbulence kinetic energy, k (J/kg), and the turbulence dissipation rate, ϵ (m²/s³), at z in the vertical profile of the dimensionless turbulent intensity, I_z , are calculated using the following equations [49]:

$$I_z = \frac{u'_z}{U_z} = 0.1 \left(\frac{z}{\delta} \right)^{-a-0.05} \quad (3)$$

$$k_z = \frac{u'_{u,z}^2 + u'_{v,z}^2 + u'_{w,z}^2}{2} \cong \frac{3}{2} u_z'^2 = \frac{3}{2} (I_z U_z)^2 \quad (4)$$

$$\epsilon_z = C_\mu^{\frac{1}{2}} k_z \frac{U_{ref}}{z_{ref}} \alpha \left(\frac{z}{z_{ref}} \right)^{\alpha-1} \quad (5)$$

where u'_z (m/s) is the root mean square of the velocity fluctuations in the stream-wise direction and $C_\mu = 0.09$ is the $k - \epsilon$ model constant.

The value of h_c is determined by the temperature difference between wall temperatures of T_s (°C) and ambient air temperature of T_a (°C). However, the FLUENT and EnergyPlus calculate the h_c differently. The

former uses the temperature of the adjacent fluid flow $T_{a,s}$ (°C) while, in contrast, EnergyPlus uses the air temperature calculated from the meteorological data at a certain height (the centroid of a surface). Therefore, to achieve a unified convective heat flux (q''_c) in both tools and to equate the two terms in the coupling process, the following equations were used:

$$q''_{c,CFD} = h_c (T_s - T_{a,s}) = h^* (T_s - T_{a,z}) = q''_{c,BES} \quad (6)$$

where h^* is the virtual h_c that enables EnergyPlus to estimate the same convection as the CFD model. This value is expressed in an iterative approach as:

$$h_{i+1}^* = \frac{q''_{c,CFD_i}}{(T_{si} - T_{a,z})} \quad (7)$$

where i specifies the current iteration index.

2.2.2. CFD model in coupling process

The CFD model is based on the Reynolds Averaged Navier Stokes (RANS) method. Using ANSYS Design Modeler and ANSYS Meshing, geometry and mesh were generated, respectively. In addition, a grid sensitivity analysis was performed to analyse the three-dimensional numerical model for which all numerical parameters and governing equations are described in detail in the following sections. The CFD model was subsequently validated against the experimental results from Ref. [49].

2.2.2.1. Computational domain and grid parameters. The computational domain was a circular model suggested by Mirzaei and Carmeliet [52] with dimensions of 5H and 15H (H is the height of the target building) in the vertical and horizontal axes, extending from the examined region, respectively, according to the COST guideline [53]. The circle's circumference was uniformly divided into 16 pieces, allowing the domain borders to capture distinct wind directions at 22.5° intervals as illustrated in Fig. 3(a).

As illustrated in Fig. 3(b), hybrid meshes were created to reduce the coupling procedure's computational cost while ensuring the accuracy [14]. Moreover, the mesh was considered as independent from the cell size, following the COST's instructions [53]. The total cell number was 700 K with the y^* within the range of 30–300 that the details were explored in the study by the authors [15].

2.2.2.2. Boundary conditions and solver setting. The vertical profiles of the mean wind speed (U), turbulent kinetic energy k , and turbulence dissipation rate ϵ for a neutrally stratified border layer of the atmosphere were defined as Eq. (1), Eq. (4) and Eq. (5), respectively, at the inflow boundary. Also, the temperature from the vertical profile was defined at

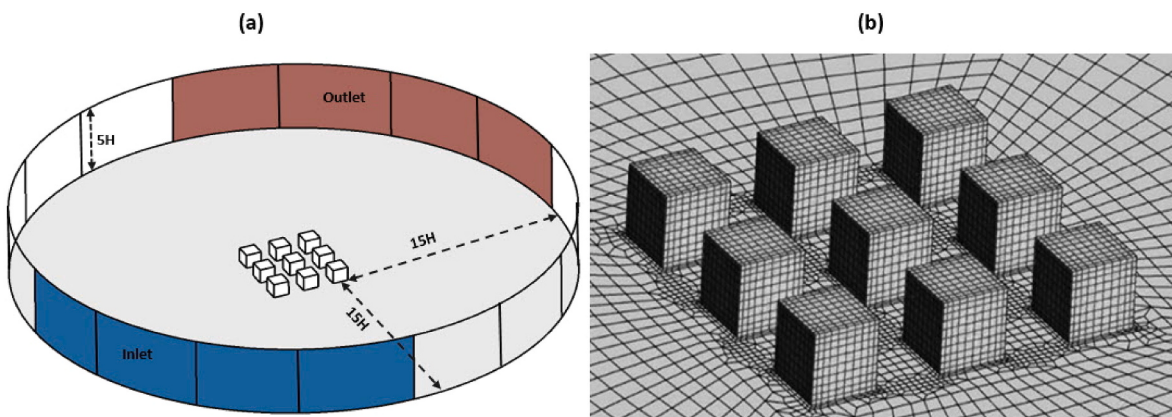


Fig. 3. (a) Computational domain and (b) mesh configuration.

this boundary. At the outflow boundary, the gauge pressure was set to zero Pa. Moreover, the no-slip condition was assigned to all wall-type boundaries and a constant temperature to the ground (T_g) which was obtained from the EnergyPlus software based on the weather data. Evidently, the building surfaces temperature (T_s) were obtained from the BES model. Furthermore, the adiabatic condition was selected for other wall-type boundaries. The turbulent model was carried out with a realizable $k - \epsilon$ steady RANS model [54] and the standard wall function. For the pressure-velocity coupling, the SIMPLE algorithm was used while the second-order discretization method was provided for both the convection and viscous elements of the governing equations.

2.2.3. CFD validation for coupling process

To validate the CFD model of the coupling method, the results of the simulations were compared with an experimental study conducted by the Architectural Institution of Japan (AIJ) [48]. The computational domain was generated similar to the model described in Section 2.2.2.1. The AIJ wind tunnel measurements provided the vertical profiles of the input velocity (U_z), kinetic energy (k_z), and turbulence dispersion rate (ϵ_z). For the wall treatment, a standard function was used. Other parameters were defined similar to those described in Section 2.2.2.2. Except for the continuity equation, which was $< 5 \times 10^{-6}$, all the equations had a convergence below six orders of magnitude.

2.3. Microclimate CFD model

The microclimate CFD model of the case study was separately simulated for each time step as summarized in Table 2 using the external surface temperature data obtained from the BES-CFD coupling's dynamic building. The same method and dimensions were followed to develop the microclimate model as described in Section 2.2.2.1. The microclimate CFD model has a different meshing method than those utilized in the coupling process; This is due to the fact that for the OTC calculation, the air velocity is required to be obtained with a higher resolution in all parts of the building block neighbourhoods while a more uniform mesh in all the streets is also more desirable. On the contrary, to reduce the computational cost in the coupling process, the layers closer to the building surfaces are required to have higher resolutions, resulting in the generation of two different meshes as explained in Section 2.2.2.1. Therefore, to maintain a grid consistency and comparability, as well as its adaptability to facilitate the assessment of the thermal comfort at equal intervals in the streets of building blocks, the grids were generated by structured cells of cutcell method inside the urban street canyons with a 1.1 expansion ratio outside the array of building block as shown in Fig. 4. The lengths of the first five layers near the target building and the ground surfaces were set as 0.01 m while the spacings between the remaining cells at the street and building levels

were set as 0.5 m y^* also fell between 30 and 300 in this case, resulting in 1,243,865 cells.

A grid sensitivity analysis was carried out for two more grids, including a coarser mesh with 0.75 m hexahedral cells within the urban street canyons (836,790 cells) and a finer mesh with 0.25 m hexahedral cells (1,895,532 cells). At distances of 2 m along a line in the perimeter of the target building, which is 2 m away from each side of the target building, as seen in Fig. 5(a) with a blue rectangle, at a height of 1.5 m above the ground, three grid's normalized wind (U/U_{ref}) were compared (Fig. 5(b)). The average deviation (e_{avg}) was found about 2% between the results of two grids, implying that the distinction between the fine and basic grids is minimal. As a result, the medium grid was envisaged to be a viable solution for anticipating the airflow within the urban neighbourhood.

To consider the buoyancy effect and use more accurate wind velocities at the pedestrian level in the outdoor thermal comfort assessment, the external surface temperature distribution of buildings retrieved from the CFD-BES coupling method was assigned to the microclimate CFD model using a user-defined function file in ANSYS Fluent. Also, to simplify the buoyancy term, Boussinesq approximation was used in this study. For the ground, the values of the roughness height $k_s = 0.3$ m and the roughness constant $C_s = 1$ (corresponding to the aerodynamic roughness length (z_0) of 0.03 m) were used in order to take the street roughness into the consideration based on the following equation:

$$k_s = \frac{9.793 z_0}{C_s} \quad (8)$$

Also, to account for the facades and roofs' roughness, the values of $k_s = 0.1$ m and $C_s = 0.5$ (corresponding to $z_0 = 0.005$ m) were outlined at the building's external surfaces. The rest of the boundary conditions and solver settings were exactly the same as those explained in Section 2.2.2.2. At this stage, the residuals' convergence thresholds were assumed to be 10^6 for the velocity components and k and 10^4 for the continuity equations.

2.4. Thermal comfort model

This study used Physiological Equivalent Temperature (PET) index to investigate the OTC in outdoor spaces as this index provides accurate and reliable results [16,55]. PET calculations were based on the Munich Energy-balance Model for Individuals (MEMI), which analyses the thermal conditions based on physiological principles of the human body [56,57]. One of the key advantages of PET is that results can be presented in °C, which makes it easier to be comprehended and compared. The numerical values of PET results were then translated to the comfort and discomfort ranges to highlight the crucial ranges in an outdoor space (see Table 3).

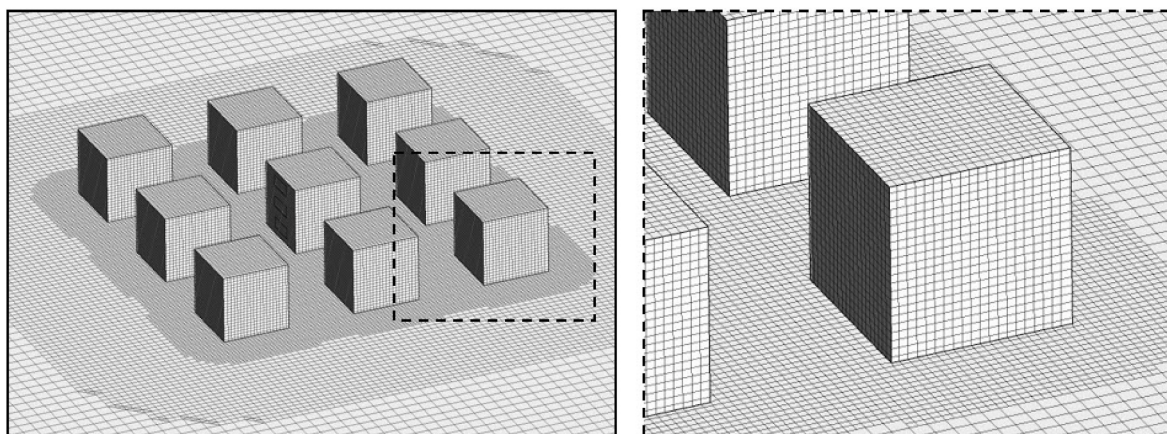


Fig. 4. Computational meshing of the microclimate CFD model.

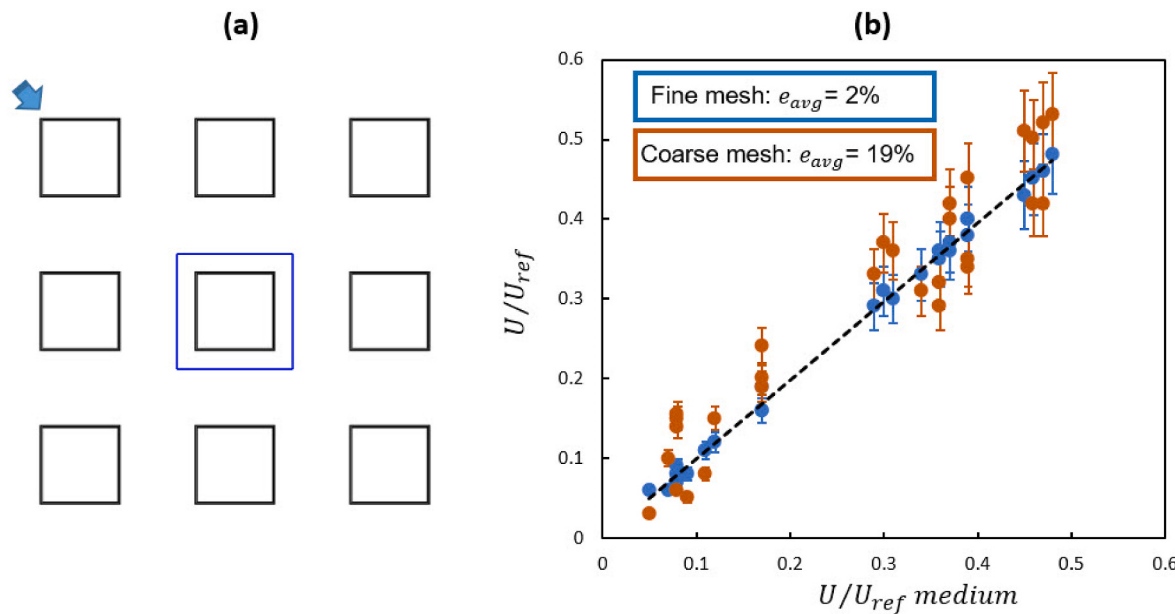


Fig. 5. (a) Representative location for the grid sensitivity study, and (b) comparison of coarse, medium, and fine grid sensitivity analysis results with lines for 10% discrepancy.

Table 3
PET sensational range associated with numerical values from calculation model [56,57].

PET comfort range	PET range (°C)
Very cold	<4
Cold	4–8
Cool	8–13
Slightly cool	13–18
Neutral	18–23
Slightly warm	23–29
Warm	29–35
Hot	35–41
Very hot	>41

As highlighted before, the proposed modelling framework calculates the OTC based on both radiant and convective heat transfer fluxes. These values are dependent on the surface temperatures of the buildings as well as the air velocities in street canyons, which are obtained from the microclimate CFD model during the period of simulation. For this purpose, the OTC model was developed in the Grasshopper platform implemented in the Rhinoceros 3D modelling software and was simulated within Ladybug and Honeybee plugins as an open-source tools [58, 59].

To simulate the PET values, the meteorological parameters are required, including air temperature, relative humidity, wind velocity, and mean radiant temperature (Tmrt) [16,55]. In the conventional PET models, these parameters are extracted from weather data files or gathered locally via comprehensive field measurements [60]. In the conventional OTC model of this study, mean radiant temperature which includes the surface temperature of buildings and ground temperature was calculated in the Grasshopper platform using an energy analysis engine (EnergyPlus) based on the weather data. While in the proposed framework, the relative humidity and air temperature were directly extracted from the weather data file (.epw) used for BES and CFD modelling (Section 2.2) while the wind velocities and buildings' external surface temperatures were transferred from the dynamic result of the BES-CFD computations (Section 2.3). The representative point coordinates of the CFD mesh were exported to a ".csv" file in order to convert the final CFD results to the OTC model, followed by importing

them into Grasshopper to be translated to the geographical points. Each cell's centre was selected as a representative location in the CFD mesh, and then the OTC results were calculated for each point to ensure an accurate coupling of BES, CFD and OTC models together. It is necessary to define the thermal properties of the outdoor ground floor to model the solar reflection from this surface that will influence the evaluation of the OTC results. Therefore, a generic outdoor floor with the asphalt material and corresponding albedo of 0.05 was defined and then the surface temperature was calculated by energy analysis engine (EnergyPlus).

To determine the efficiency of the proposed framework over the former approach, two tempo-spatial OTC models were developed, including one model based on the conventional OTC calculation methodology (standalone OTC model) and the other one, based on the BES-CFD-OTC coupled model. To compare the performance of these two models, a tempo-spatial metric, Weighted Temporal Comfort Performance (TCP_w), was employed to investigate the thermal comfort in outdoor areas. Hence, TCP_w is used to evaluate the OTC score temporally for each point of the simulation grid during a defined time period [44]. The application and validity of this metric in the neighbourhood scale were investigated in the previous study [60]. TCP_w is defined as below:

$$TCP_w = \frac{1}{d} \frac{1}{h} \sum_{i=1}^d \sum_{j=1}^h TC_{ij} \quad (9)$$

where TC_{ij} is the timely averaged of the thermal comfort score at each point and displays the thermal comfort score of a location during a certain hour (h) on a particular day (d) of a year. The TCP_w equals 1.0 when a point is inside the comfort range according to Eq. (9), and when it is outside of this range, the deviation from the comfort range can be computed as follows:

$$TC_{ij} = \begin{cases} 1 & \text{if } C_{min} \leq T_{ij} \leq C_{max} \\ \frac{\Delta T_{comf}}{\Delta T_{ij}} & \text{otherwise} \end{cases} \quad (10)$$

where C_{min} and C_{max} are defined as the maximum and minimum thresholds of the acceptable comfort range. ΔT_{comf} is the acceptable comfort range's amplitude (Eq. (11)), and ΔT_{ij} denotes the absolute difference between the local thermal comfort value at each point (T_{ij}) and the comfort range's midpoint:

$$\Delta T_{comf} = \frac{C_{max} - C_{min}}{2}$$

$$\Delta T_{ij} = \left| T_{ij} - \left(\frac{C_{max} + C_{min}}{2} \right) \right| \quad (11)$$

In this study, the acceptable comfort range was determined by utilizing PET as the OTC index. This index specifies the method for computing T_{ij} of a location at a specific time as well as the comfort range, C_{min} and C_{max} , which were 18 °C and 23 °C accordingly (Table 3). As it is presented by Eq. (10), if the value of TCP_w is closer to 1, a higher range of thermal comfort can be obtained at that point during the simulation period. The TCP_w index analyses the temporal performance of the OTC at each point and the tempo-spatial performance can be derived by repeating the calculation for each point in the simulation area.

3. Results

3.1. Microclimate CFD validation

As explained in Section 2.3, a different meshing method was utilized than those employed in the coupling process. Hence, to ensure that the microclimate CFD model is consistent with the one employed in the coupling process, the results of the experimental wind tunnel study by AIJ-case C [48] were used again to validate the microclimate CFD model. With the exception of the meshing method, all parameters and settings of both CFD models were kept exactly similar as explained in Section 2.2.3.

Besides, to validate both CFD simulation method, the experimental results of wind velocity at 0.02 m above the ground normalized against the approaching wind velocity at 0.2 m height at various positions on the wind tunnel model was compared with the wind velocities calculated from both CFD models. As reported in Ref. [15], the mean relative error of the developed CFD model for the coupling CFD and BES process and experimental results was approximately 13%, which was considered as satisfactory.

Validation results for the microclimate CFD model in half of the points (Fig. 6(a)) are illustrated in Fig. 6(b), which indicated an average deviation of about 11%, which is again within an acceptable range [52]. This implies that the grid resolution is suitable to accurately simulate the airflow within the urban neighbourhood.

3.2. Surface temperature from BES-CFD coupling

Fig. 7 compares the target central buildings' exterior wall temperature contours by BES-only and BES-CFD coupling methods. As can be seen from this figure, in general, the coupled roof temperature is found

slightly higher than that by the BES-only method. However, on the contrary to that, the temperature of the vertical walls by the coupling methods is found lower than that by the BES-only method. When separately considering walls of different orientations, denoting south, east, north, and west walls as S1, S2, S3, and S4, respectively, the impact of the local airflow can be explored as explained in the following paragraphs.

At 6:00, when there was no impact of solar radiation and the wind angle was 70°, approaching from a north-east direction, the algorithm of EnergyPlus considered S2s (east walls) as the windward walls while other walls as the leeward. Thereby, the standard deviation of all S2s by BES-only is much smaller (approximately 0.07) compared to those of other walls having similar standard deviations within the range of 0.23–0.29. However, the coupling method deals with the local airflow related to this case. It gives the windward S2s a standard deviation of 0.22, their opposite leeward S4s of 0.3, and the lateral S1s and S3s of 0.12 and 0.13, respectively.

The wind was from due West at the noon. The standard deviations of S2s and S3s by the coupling method are approximately twice as those by the BES-only method. At S1s, where surfaces facing south are lit up and heated to a very high temperature (over 54 °C), the standard deviation of temperature by the BES-only becomes higher than that by the coupling method. For the west-facing S4s, which supposed to perform similarly to S2s if only the impact of radiation has been considered, the standard deviation of the surface temperature by the coupling method is very smaller than that by the BES-only method, 0.05 compared to 0.28 indeed due to the breeze coming from the West direction with a velocity of 4.6 m/s.

In two similar scenarios at 18:00 and 24:00, winds come from southwest direction at 230° and 220° with the velocities of 3.1 m/s and 2.1 m/s. There is entirely the wind impact on the surface temperature at 24:00 while solar radiation is still affecting when the sunset is at 18:00 though the radiation is quite low; thus, wind is considered as the dominating factor.

The average deviation between the envelope temperature through 25th Sep. by the BES-only and BES-CFD coupling methods is approximately 1.1 °C, with the highest value up to 6.5 °C, occurring on the west wall of the top floor at 16:00. This highlights the importance of the neighbourhood effect on a combined impact of the radiative and convective heat fluxes.

In Fig. 8, the results of outdoor surface temperature from the BES-only and BES-CFD coupling methods are also compared for all solid walls and roof of the central target building for four selected times in the studied day. The defined format is used to identify each surface while the floor number (F) is followed by the surface orientation (S). Also, the roof of the building is presented by R) and the window by W. Then,

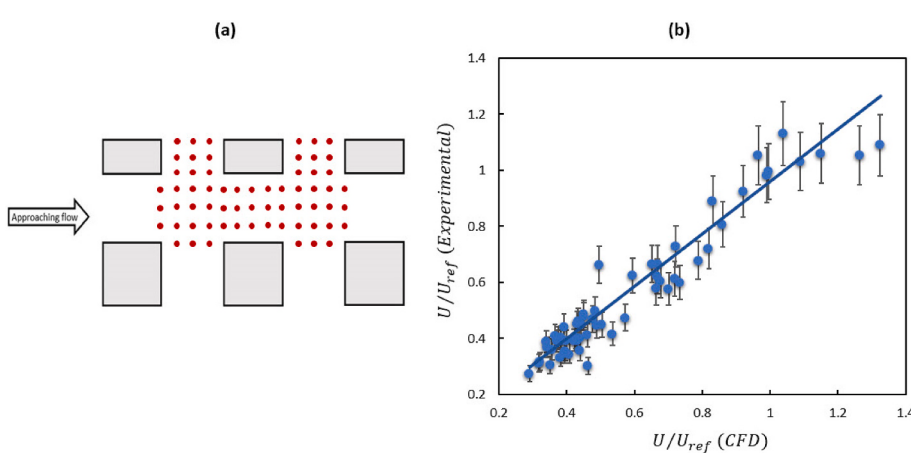


Fig. 6. (a) The validation study's representative points used in the wind tunnel measurements (AIJ), and (b) comparison of the normalized wind velocities between the experiment and CFD model with lines for 10% discrepancy.

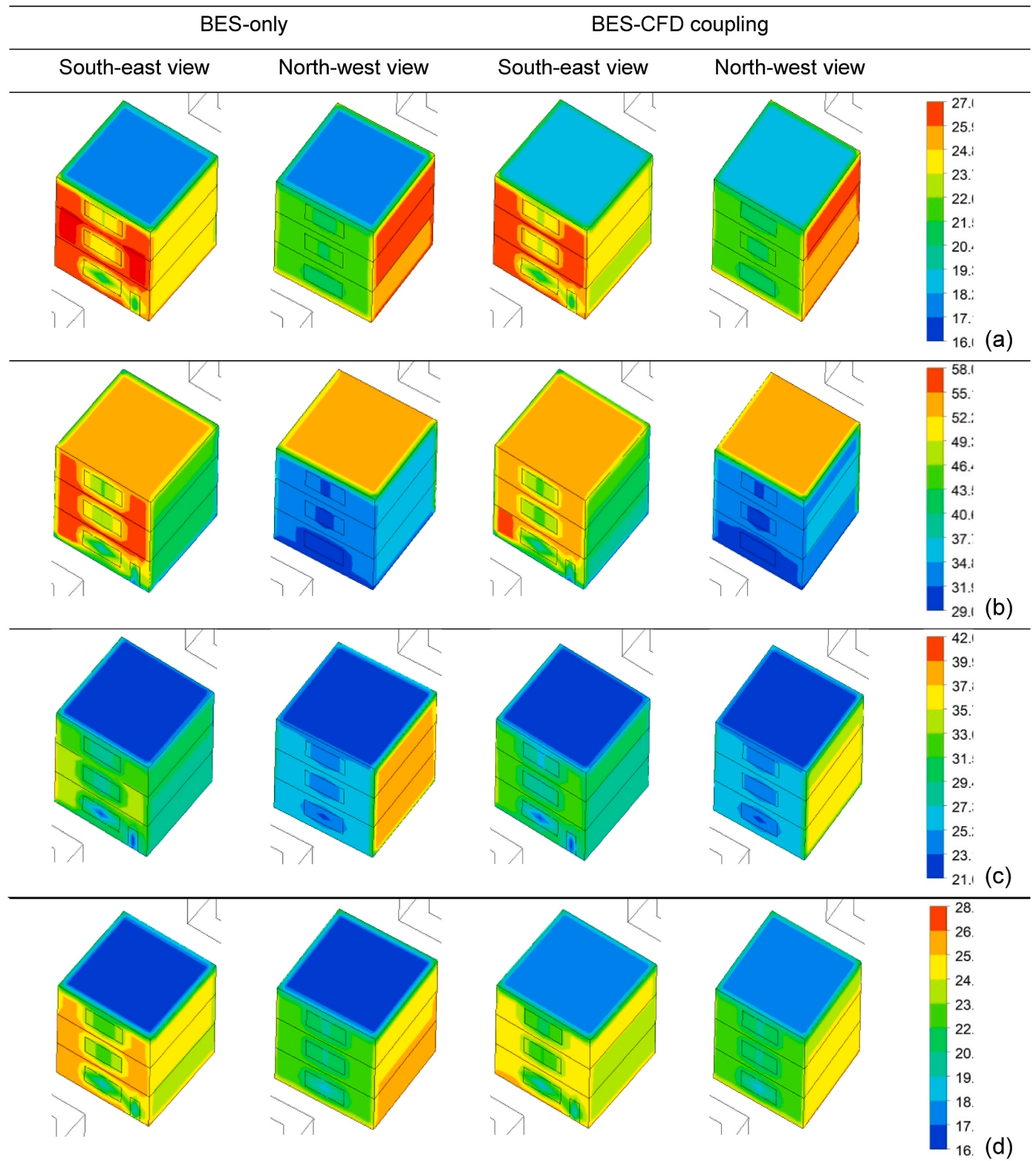


Fig. 7. Comparison of temperature contours of the central target building by BES-only and BES-CFD coupling methods at (a) 6:00, (b) 12:00., (c) 18:00 and (d) 24:00 of 25th Sep.

starting from due south, all surfaces are labelled in a counter-clockwise manner from 1 (e.g., F1S2 denotes the east wall on the ground floor). As it can be noticed in these figures, the temperature difference is greater against the windward surfaces, which are more affected by the wind flow; the higher the wind velocity, the greater the surface temperature

difference. For example, at the time of 9:00 with a wind velocity of 2.1 m/s, the surface temperature at F2S2, which belongs to the east wall (windward surface) on the second floor, is about 2.5 °C lower in the coupling method than those achieved from BES-only (Fig. 8). Similarly, at 16:00 with 5.7 m/s velocity, these differences at S1 and S4 as

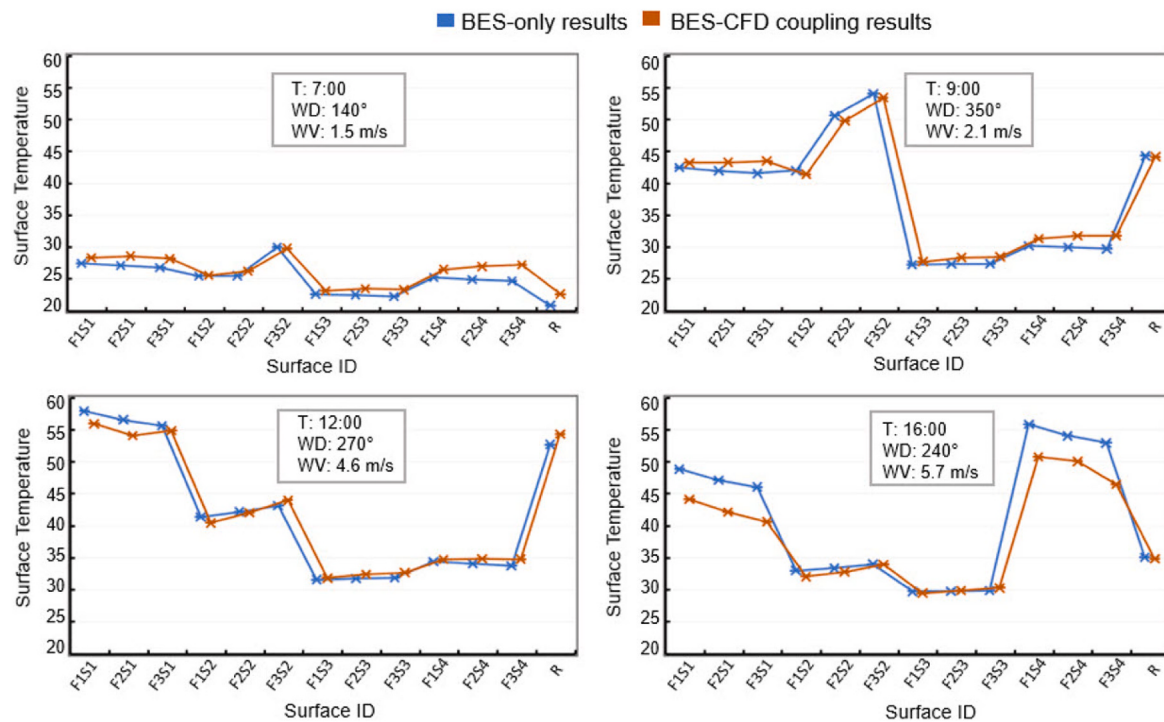


Fig. 8. Comparison of external surface temperatures between BES and BES-CFD coupling method at four time with assigned wind direction (WD) and wind velocity (WV).

windward surfaces are about 5 °C–6.5 °C as seen in Fig. 8. This highlights a significant impact of the airflow patterns and convective fluxes on the temperature of the external surfaces.

Fig. 9(a) compares the external surface's temperatures achieved from BES-only and BES-CFD coupling methods, and Fig. 9(b) illustrates this comparison for the glazing surface's temperatures. These figures show that, when compared to the solid surfaces, the surface temperature distribution pattern of the windows is substantially smaller. The solid surfaces have temperatures ranging from 20 °C to 60 °C, while the windows have temperatures ranging from 20 °C to 36 °C. This demonstrates that the materials have a substantial impact on the surface temperatures. Also, it is clear that glazing surface temperatures are less sensitive to the choice of simulation method since the temperature difference is smaller (Fig. 9).

3.3. Microclimate CFD simulation results

For the duration from 7:00–18:00 on 25th of September according to the meteorological data, 12 CFD simulations (see Table 2) are performed

to achieve the hourly wind velocities according to the climatic condition of Los Angeles and time-variant building surface temperature calculated in BES-CFD coupling method as defined as Step-2 in the proposed framework. In the studied interval, the minimum and maximum wind velocities are 1.5 m/s and 5.7 m/s, respectively.

The velocity contours at the corresponding time and wind direction in the selected day at 1.5 m above ground are depicted in Fig. 10. It can be seen that the flow pattern changes against different wind directions across the street canyons. The average air velocity increases in the corners of the first row of buildings facing the wind while the wind velocity gradually decreases along the next row of buildings. Also, the low-pressure areas are formed against the lower wind velocities behind the buildings.

Fig. 11 illustrates the air velocity results achieved from CFD simulation associated to the cases shown in Fig. 10 at the height of 1.5 m above the ground along a line shown in Fig. 5(a). The distribution of the air velocity values from the microclimate CFD model at different points depends on the wind direction. As shown in Fig. 11, there is a maximum difference of about 1.6 m/s between minimum and maximum air

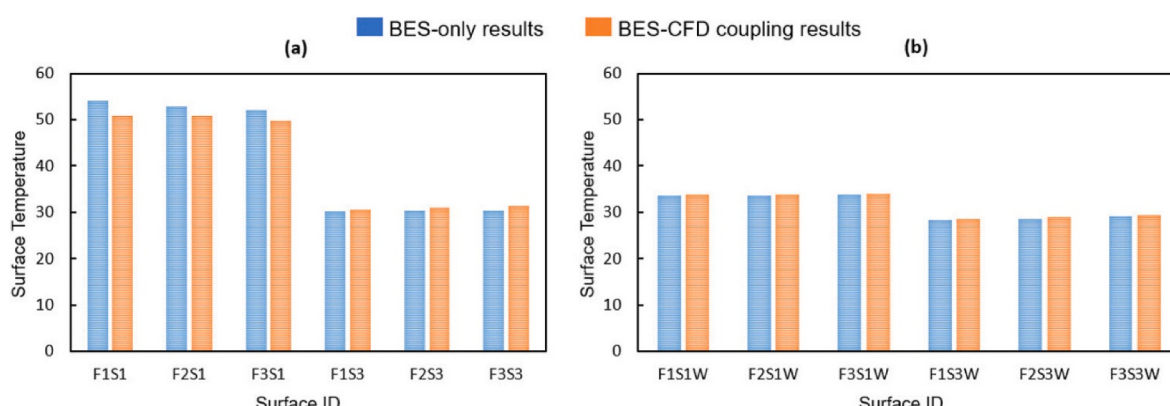


Fig. 9. (a) Solid and (b) glazing surface temperatures achieved from BES-only and BES-CFD coupling method.

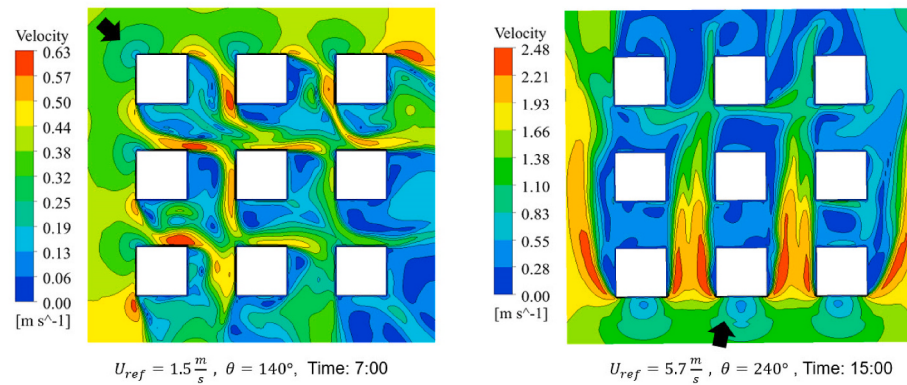


Fig. 10. Velocity contours of minimum and maximum wind speeds with corresponding wind direction at 1.5 m above the ground.

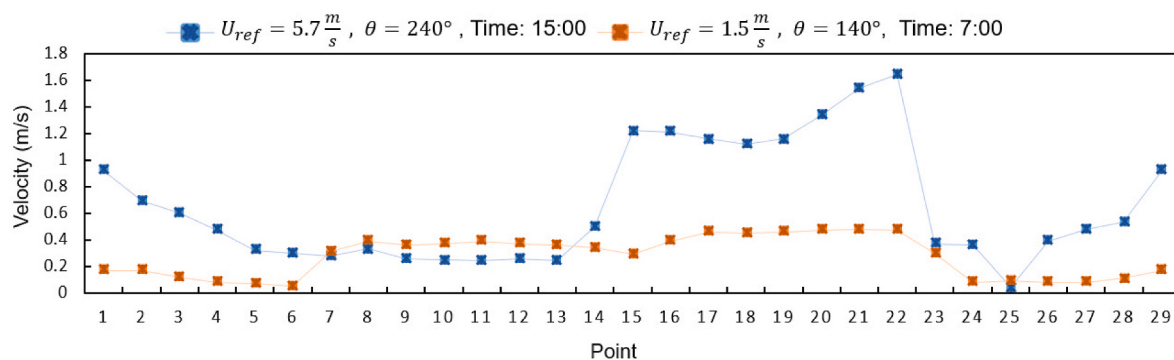


Fig. 11. Air velocity results of CFD simulation in two different hours on the studied day around the central building.

velocity results along the selected line for the reference air velocity of 5.7 m/s and wind direction of 240° . This value is about 0.5 m/s for the reference wind of 1.5 m/s and wind direction of 140° . In other words, the difference between the minimum and maximum air velocity results is greater at the higher air velocities. This considerable difference in the air velocity in the neighbourhood contexts highlights a significant impact of the airflow patterns and convective fluxes on the OTC investigations.

3.4. Thermal comfort analysis

Fig. 12 shows the distribution of PET values for simulation points provided by the coupled model and the standalone OTC model. The split violin diagram depicts the summary statistics (mean, quantiles, and outliers) and the kernel density of PET at three different times of the simulation day (morning, noon and afternoon) to capture the temporal-spatial performance of the proposed framework. The distribution trend for both OTC models is quite consistent but comparing quantiles'

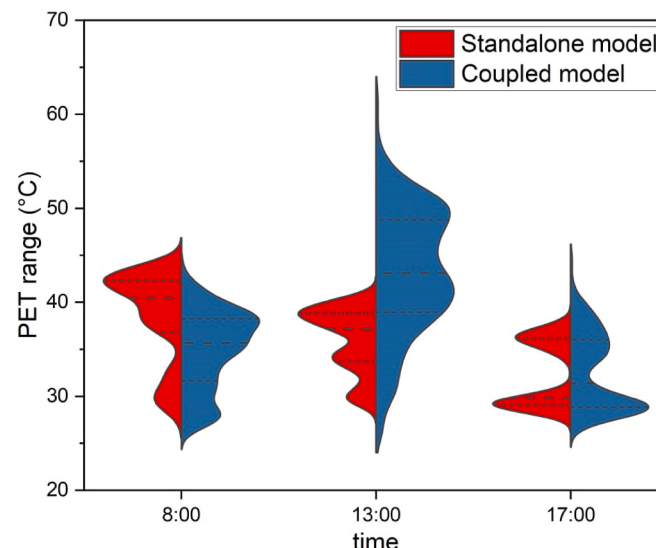


Fig. 12. Distribution of PET values calculated within simulation points for standalone and coupled OTC models.

lengths highlights the fact that the OTC values in the coupled model are scattered in a broader range. For example, at 13:00, the PET values of the coupled model, are within a range of 23 °C–58 °C while in the standalone model, these values vary from 23 °C to 44 °C. In the coupled model, PET quantiles are more stretched out towards the upper values, representing both a wider variety and higher PET values (more discomfort and heat stress ranges). Similarly, at 17:00, the PET values of the standalone model start from 28 °C to 40 °C while the upper limit in the coupled model rises up to 47 °C; nevertheless, the kernel probability patterns of both models are similar to each other.

To grasp a more detailed picture of the OTC tempo-spatial performance, a couple of critical geographical points from the representative grid points are selected to depict the differences between standalone and coupled models in more details. As such, four points with a 1.5 m distance to the south surface of the centre building, and with a similar distance of 4 m from each other are chosen (Fig. 13(a)) to highlight the tempo-spatial variation of OTC during the simulation day. Fig. 13 shows that there is a significant difference between the temporal pattern of PET values obtained from these two models. In the standalone model, there is no significant difference between the calculated PET values during a day (Fig. 13(b)) while the general patterns in Fig. 13(c) present new peak points (13:00 to 14:00). Also, each point experiences a wider range of PET values in a day, which can be observed in Fig. 12. The other differences are related to the comfort level in the morning times in which PET values in the standalone model are higher (Fig. 13(b)) compared to the noon time while this pattern is inverse in the coupled model (Fig. 13(c)).

The tempo-spatial performance of the standalone and coupled OTC models is assessed by using a histogram of TCP_w values at the simulation points based on Eqs. 9–11 as depicted in Fig. 14. This index shows the total OTC score of each point during the period of 7:00–18:00. The distribution of TCP_w for the coupled model is more diverse and is leaning toward lower values at the TCP_w spectrum, which implies a more

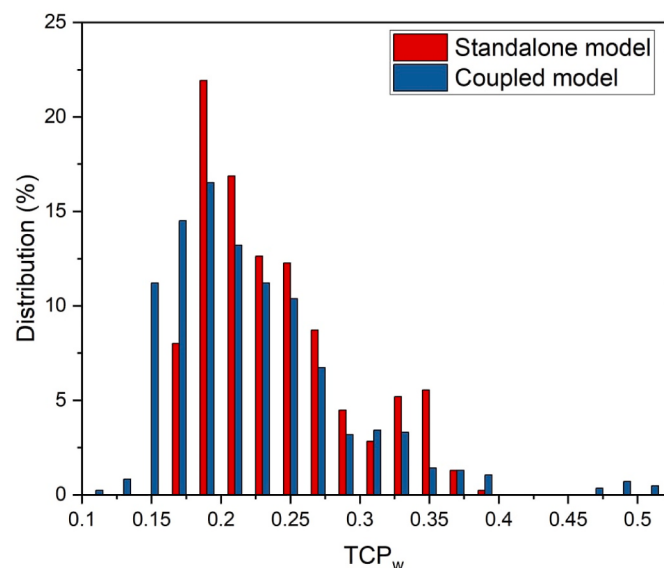


Fig. 14. The occurrence rate of TCP_w for simulation points in the period of 7:00–18:00 by means of histograms (the higher TCP_w values show a higher level of comfort performance).

deviation from the comfort range. These trends are in agreement with the findings shown in Fig. 12. Results of this analysis also reveal that a substantial fraction of the locations in the case study falls within the range of 0.18–0.25, which is a significant deviation from the comfort range. In fact, the density of the columns of the coupled model on the left side of Fig. 14 indicates that this model has a higher number of spatial points with a lower comfort level. However, the distribution trend of TCP_w at the standalone model is not similar with a higher percentage of

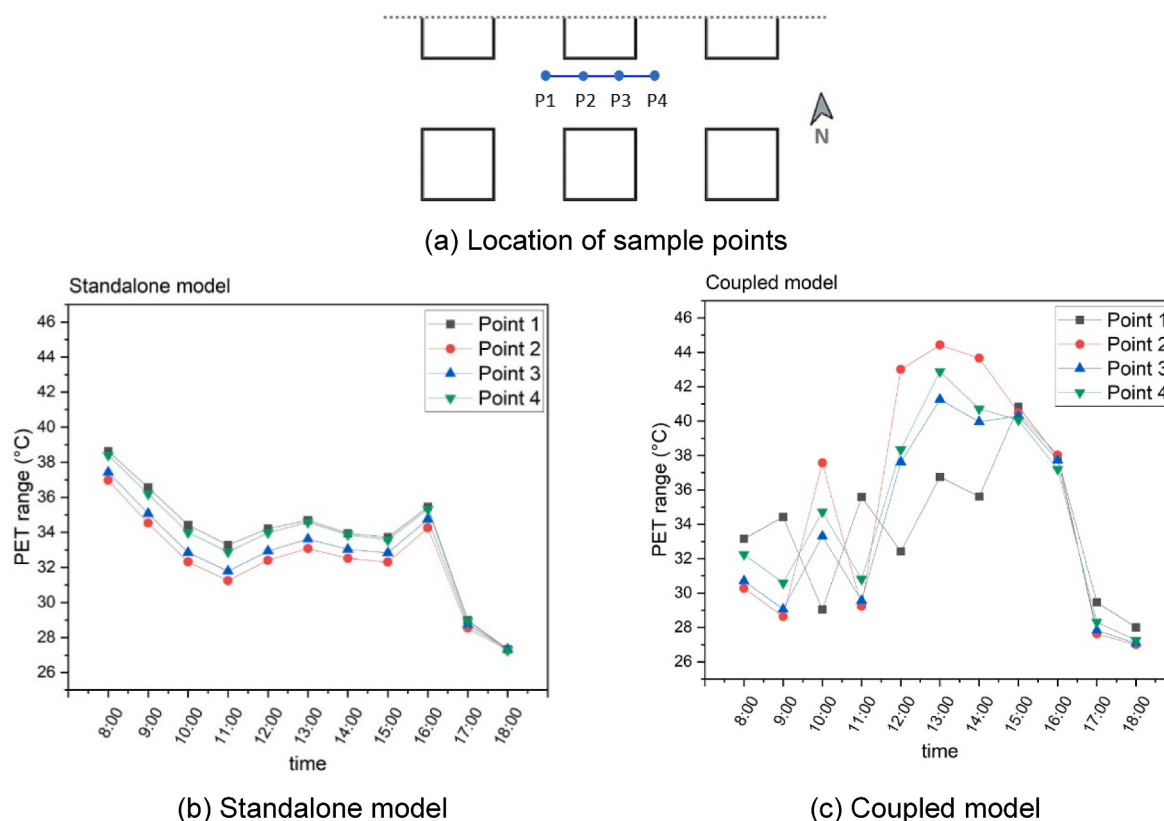


Fig. 13. Temporal pattern of PET values calculated for sample points mentioned above based on standalone and coupled OTC models.

points located on the right side of the histogram, indicating a higher comfort level.

The coupling framework highlights the difference between the results of these two models. In total, the average value of OTC in the coupled model is 6.5% higher compared to the standalone model. Also, tempo-spatial analysis reveals that the difference pattern of results between these two models is not the same during the whole day, for instance, in the morning time, the average of OTC difference is 8.7% while this value is significantly higher at noon as it reaches up to 13.5% and decreases again to 3.5% in the afternoon. These findings emphasise on the importance and impact of this coupling process in the tempo-spatial modelling of OTC on the neighbourhood scale.

4. Conclusions

For the OTC assessment, it is critical to simultaneously consider the effect of both radiative and convective fluxes. In this study, a novel and step by step framework is proposed that incorporates the buildings' external surface temperatures obtained from a dynamic BES-CFD coupling approach, wind velocity from a microclimate CFD model, and solar radiation from Honeybee software. The major conclusions of this study are as follows:

- The surface temperature (T_s) anticipated by the BES tool and the CHTC (q_c'') projected by the CFD tool are shared between the BES and CFD domains after achieving a sufficient agreement on the convective heat flux values between two domains.
- In the BES-CFD coupling approach, the predicted external surface temperatures of a building experience a higher variation at those surfaces mostly affected by wind, which are about 6.5 °C and 2.5 °C for the reference wind velocities of 5.7 m/s and 2.1 m/s, respectively.
- The air velocity in most of the points calculated in the CFD model is lower than that achieved by the logarithmic profile due to the sheltering effect of the neighbourhood geometry, especially in the normal wind directions where more wake regions are created. During the calculated hours, the maximum velocity differences of 0.35 m/s and 1.4 m/s are observed against the reference velocities of 2.1 m/s and 5.7 m/s, respectively.
- Integration of air velocity values from the microclimate CFD model, the surface temperature from the BES-CFD coupling method, and solar radiation from Honeybee in the proposed tempo-spatial OTC modelling framework can significantly change the OTC results; this varies depending on the daytime, wind velocity, wind direction, and study points' locations.
- In terms of spatial distribution, the OTC results of the coupled model are more scattered in different locations compared to the standalone model, and they represent a greater range. Also, the higher PET values leaning towards discomfort and heat stress range, highlighting the significance and impact of the proposed coupling process.
- In terms of temporal distribution, a similar pattern is observed. The temporal PET values from coupled model experience a wider range during the studied day with a pick point of 45 °C at 13:00 while no significant difference amongst the calculated PET values was observed in the standalone method with 39.5 °C pick point at 8:00.
- A substantial number of locations in this case study have a significant deviation from the comfort range, especially in the coupled model, since the distribution of T_{CP_w} is leaning toward the lower values that results in a lower comfort level. This point highlights the fact that the standalone OTC models tend to show comfort range in some locations where with a more accurate calculation method, they will be considered in the heat stress and discomfort zones.

This proposed framework is repeatable and is location- and design-independent. However, there are some limitations such as considering a constant ground surface temperature applied in the CFD simulations

based on the weather data that do not consider the building's shadow, which can affect the air velocity results. Moreover, building surface temperatures obtained from BES have a low spatial resolution based on Fig. 7. BES tools mostly provide a uniform value over large wall surfaces, which might be leading to an underestimation of the impact of microclimate impact since a high-resolution convective heat flux from CFD is averaged. Furthermore, future studies should integrate the dynamic impact of other CFD-based meteorological parameters such as air temperature and humidity into OTC framework. Also, these studies are required to evaluate this framework for the larger-scale urban areas and for more complex neighbourhoods' geometry using a broader variety of details and materials used in the building envelopes' construction.

CRediT authorship contribution statement

Marzieh Fallahpour: Writing – original draft, Validation, Methodology, Conceptualization. **Reihaneh Aghamolaei:** Writing – original draft, Methodology, Conceptualization. **Ruijun Zhang:** Writing – original draft, Methodology, Conceptualization. **Parham A. Mirzaei:** Writing – review & editing, Supervision, Methodology, Conceptualization.

Declaration of competing interest

The authors declare that they have no known competing financial interests or personal relationships that could have appeared to influence the work reported in this paper.

Data availability

Data will be made available on request.

References

- [1] G. Roshan, M. Moghbel, S. Attia, Evaluating the wind cooling potential on outdoor thermal comfort in selected Iranian climate types, *J. Therm. Biol.* 92 (2020), 102660, <https://doi.org/10.1016/j.jtherbio.2020.102660>.
- [2] S. Banerjee, S. Chattopadhyay, A meta-analytical review of outdoor thermal comfort research: applications, gaps and a framework to assess low-income settlements in Indian megacities, *Urban Clim.* 33 (2020), 100641, <https://doi.org/10.1016/j.uclim.2020.100641>.
- [3] R. Aghamolaei, A. Lak, Outdoor thermal comfort for active ageing in urban open spaces: reviewing the concepts and parameters, *Ageing Int.* (2022) 1–14, <https://doi.org/10.1007/s12126-022-09482-w>.
- [4] P.A. Mirzaei, R. Aghamolaei, The hot climate of the Middle East, in: *Advances in 21st Century Human Settlements*, Springer, Singapore, 2021, pp. 205–234, https://doi.org/10.1007/978-981-33-4050-3_10.
- [5] S. Yoo, K. Ito, Multi-stage optimization of local environmental quality by comprehensive computer simulated person as a sensor for HVAC control, *Adv. Build. Energy Res.* 14 (2020) 171–188, <https://doi.org/10.1080/17512549.2019.1588167>.
- [6] L. Malys, M. Musy, C. Inard, Microclimate and building energy consumption: study of different coupling methods, *Adv. Build. Energy Res.* 9 (2015) 151–174, <https://doi.org/10.1080/17512549.2015.1043643>.
- [7] R. Aghamolaei, M.M. Azizi, B. Aminzadeh, J. O'Donnell, A comprehensive review of outdoor thermal comfort in urban areas: effective parameters and approaches, *Energy Environ.* (2022), <https://doi.org/10.1177/0958305X221116176>, 0958305X2211161.
- [8] F. Bourbia, F. Boucheriba, Impact of street design on urban microclimate for semi arid climate (Constantine), *Renew. Energy* 35 (2010) 343–347, <https://doi.org/10.1016/J.RENENE.2009.07.017>.
- [9] J.A. Acero, L.A. Ruefenacht, E.J.Y. Koh, Y.S. Tan, L.K. Norford, Measuring and comparing thermal comfort in outdoor and semi-outdoor spaces in tropical Singapore, *Urban Clim.* 42 (2022), 101122, <https://doi.org/10.1016/j.uclim.2022.101122>.
- [10] S. Khalili, R. Fayaz, S.A. Zolfaghari, Analyzing outdoor thermal comfort conditions in a university campus in hot-arid climate: a case study in Birjand, Iran, *Urban Clim.* 43 (2022), 101128, <https://doi.org/10.1016/j.uclim.2022.101128>.
- [11] G. Evola, V. Costanzo, C. Magri, G. Margani, L. Marletta, E. Naboni, A novel comprehensive workflow for modelling outdoor thermal comfort and energy demand in urban canyons: results and critical issues, *Energy Build.* 216 (2020), 109946, <https://doi.org/10.1016/j.enbuild.2020.109946>.
- [12] P.K. Cheung, C.Y. Jim, Subjective outdoor thermal comfort and urban green space usage in humid-subtropical Hong Kong, *Energy Build.* 173 (2018) 150–162, <https://doi.org/10.1016/j.enbuild.2018.05.029>.

- [13] D. Lai, C. Zhou, J. Huang, Y. Jiang, Z. Long, Q. Chen, Outdoor space quality: a field study in an urban residential community in central China, *Energy Build.* 68 (2014) 713–720.
- [14] R. Zhang, P.A. Mirzaei, J. Carmeliet, Prediction of the surface temperature of building-integrated photovoltaics: development of a high accuracy correlation using computational fluid dynamics, *Sol. Energy* 147 (2017) 151–163, <https://doi.org/10.1016/j.solener.2017.03.023>.
- [15] R. Zhang, P.A. Mirzaei, B. Jones, Development of a dynamic external CFD and BES coupling framework for application of urban neighbourhoods energy modelling, *Build. Environ.* 146 (2018) 37–49, <https://doi.org/10.1016/j.buildenv.2018.09.006>.
- [16] R. Aghamolaei, M. Fallahpour, P.A. Mirzaei, Tempo-spatial thermal comfort analysis of urban heat island with coupling of CFD and building energy simulation, *Energy Build.* 251 (2021), 111317, <https://doi.org/10.1016/J.ENBUILD.2021.111317>.
- [17] X. Lu, A.M. Memari, Determination of exterior convective heat transfer coefficient for low-rise residential buildings, *Adv. Build. Energy Res.* 15 (2021) 583–602, <https://doi.org/10.1080/17512549.2019.1612468>.
- [18] R. Zhang, P.A. Mirzaei, Virtual dynamic coupling of computational fluid dynamics-building energy simulation-artificial intelligence: case study of urban neighbourhood effect on buildings' energy demand, *Build. Environ.* 195 (2021), 107728, <https://doi.org/10.1016/j.buildenv.2021.107728>.
- [19] M. Akbari Paydar, Optimum design of building integrated PV module as a movable shading device, *Sustain. Cities Soc.* 62 (2020), 102368, <https://doi.org/10.1016/j.scs.2020.102368>.
- [20] D.B. Crawley, J.W. Hand, M. Kummert, B.T. Griffith, Contrasting the capabilities of building energy performance simulation programs, *Build. Environ.* 43 (2008) 661–673, <https://doi.org/10.1016/J.BUILDENV.2006.10.027>.
- [21] C.O.R. Negrião, Integration of computational fluid dynamics with building thermal and mass flow simulation, *Energy Build.* 27 (1998) 155–165, [https://doi.org/10.1016/s0378-7788\(97\)00036-4](https://doi.org/10.1016/s0378-7788(97)00036-4).
- [22] M.G. Emmel, M.O. Abadie, N. Mendes, New external convective heat transfer coefficient correlations for isolated low-rise buildings, *Energy Build.* 39 (2007) 335–342, <https://doi.org/10.1016/j.enbuild.2006.08.001>.
- [23] M. Aminipour, A.J. Knudby, E.S. Krayenhoff, K. Zickfeld, A. Middel, Modelling the Impact of Increased Street Tree Cover on Mean Radiant Temperature across Vancouver's Local Climate Zones, vol. 39, *Urban For Urban Green*, 2019, pp. 9–17, <https://doi.org/10.1016/j.ufug.2019.01.016>.
- [24] E. Naboni, M. Meloni, S. Cocco, J. Kaempf, J.L. Scartezzini, An overview of simulation tools for predicting the mean radiant temperature in an outdoor space, in: *Energy Procedia*, Elsevier, 2017, pp. 1111–1116, <https://doi.org/10.1016/j.egypro.2017.07.471>.
- [25] M.H. Elnabawi, N. Hamza, S. Dudek, Use and evaluation of the envi-met model for two different urban forms in cairo, Egypt: measurements and model simulations, in: *Proceedings of BS 2013: 13th Conference of the International Building Performance Simulation Association*, 2013, pp. 2800–2806.
- [26] X. Liu, Y. Ming, Y. Liu, W. Yue, G. Han, Influences of landform and urban form factors on urban heat island: comparative case study between Chengdu and Chongqing, *Sci. Total Environ.* 820 (2022), 153395, <https://doi.org/10.1016/j.scitotenv.2022.153395>.
- [27] M. Zinzi, S. Agnoli, C. Burattini, B. Matttoni, On the thermal response of buildings under the synergic effect of heat waves and urban heat island, *Sol. Energy* 211 (2020) 1270–1282, <https://doi.org/10.1016/j.solener.2020.10.050>.
- [28] S.J. Mei, C. Yuan, Urban buoyancy-driven air flow and modelling method: a critical review, *Build. Environ.* 210 (2022), 108708, <https://doi.org/10.1016/j.buildenv.2021.108708>.
- [29] P.A. Mirzaei, Recent challenges in modeling of urban heat island, *Sustain. Cities Soc.* 19 (2015) 200–206, <https://doi.org/10.1016/j.scs.2015.04.001>.
- [30] G. Heidarinejad, S. Shokrollahi, H. Pasdarshahri, An investigation of thermal comfort, IAQ, and energy saving in UFAD systems using a combination of Taguchi optimization algorithm and CFD, *Adv. Build. Energy Res.* 15 (2021) 799–817, <https://doi.org/10.1080/17512549.2020.1784276>.
- [31] R. Zhang, Y. Gan, P.A. Mirzaei, A new regression model to predict BIPV cell temperature for various climates using a high-resolution CFD microclimate model, *Adv. Build. Energy Res.* 14 (2020) 527–549, <https://doi.org/10.1080/17512549.2019.1654917>.
- [32] M. Shirzadi, M. Naghashzadegan, P.A. Mirzaei, Improving the CFD modelling of cross-ventilation in highly-packed urban areas, *Sustain. Cities Soc.* 37 (2018) 451–465, <https://doi.org/10.1016/j.scs.2017.11.020>.
- [33] P.A. Mirzaei, F. Haghishat, A novel approach to enhance outdoor air quality: pedestrian ventilation system, *Build. Environ.* 45 (2010) 1582–1593, <https://doi.org/10.1016/j.buildenv.2010.01.001>.
- [34] P.A. Mirzaei, F. Haghishat, Pollution removal effectiveness of the pedestrian ventilation system, *J. Wind Eng. Ind. Aerod.* 99 (2011) 46–58, <https://doi.org/10.1016/j.jweia.2010.10.007>.
- [35] M. Shirzadi, P.A. Mirzaei, M. Naghashzadegan, Y. Tominaga, Modelling enhancement of cross-ventilation in sheltered buildings using stochastic optimization, *Int. J. Heat Mass Tran.* 118 (2018) 758–772, <https://doi.org/10.1016/j.ijheatmasstransfer.2017.10.107>.
- [36] X. Wang, Y. Li, Predicting urban heat island circulation using CFD, *Build. Environ.* 99 (2016) 82–97, <https://doi.org/10.1016/j.buildenv.2016.01.020>.
- [37] J. Allegri, V. Dorer, J. Carmeliet, Coupled CFD, radiation and building energy model for studying heat fluxes in an urban environment with generic building configurations, *Sustain. Cities Soc.* 19 (2015) 385–394, <https://doi.org/10.1016/j.scs.2015.07.009>.
- [38] M. Shirzadi, P.A. Mirzaei, M. Naghashzadegan, Development of an adaptive discharge coefficient to improve the accuracy of cross-ventilation airflow calculation in building energy simulation tools, *Build. Environ.* 127 (2018) 277–290, <https://doi.org/10.1016/j.buildenv.2017.10.019>.
- [39] S. Gilani, H. Montazeri, B. Blocken, CFD simulation of stratified indoor environment in displacement ventilation: validation and sensitivity analysis, *Build. Environ.* 95 (2016) 299–313, <https://doi.org/10.1016/j.buildenv.2015.09.010>.
- [40] P.A. Mirzaei, F. Haghishat, Approaches to study urban heat island - abilities and limitations, *Build. Environ.* 45 (2010) 2192–2201, <https://doi.org/10.1016/j.buildenv.2010.04.001>.
- [41] M.G. Davies, *Building Heat Transfer*, wiley, 2006, <https://doi.org/10.1002/0470020555>.
- [42] J.A. Palyvos, A survey of wind convection coefficient correlations for building envelope energy systems' modeling, *Appl. Therm. Eng.* 28 (2008) 801–808, <https://doi.org/10.1016/j.applthermaleng.2007.12.005>.
- [43] A. de L. Vollaro, G. Galli, A. Vallati, CFD analysis of convective heat transfer coefficient on external surfaces of buildings, *Sustainability* 7 (2015) 9088–9099, <https://doi.org/10.3390/su7079088>.
- [44] N. Nazarian, J. Fan, T. Sin, L. Norford, J. Kleissl, Predicting outdoor thermal comfort in urban environments: a 3D numerical model for standard effective temperature, *Urban Clim.* 20 (2017) 251–267, <https://doi.org/10.1016/j.ulclim.2017.04.011>.
- [45] S. Charisi, M. Waszczuk, T.K. Thisis, Determining building-specific wind pressure coefficients to account for the microclimate in the calculation of air infiltration in buildings, *Adv. Build. Energy Res.* 15 (2021) 368–389, <https://doi.org/10.1080/17512549.2019.1596835>.
- [46] Y. Toparlar, B. Blocken, B. Maiheu, G.J.F. van Heijst, Impact of urban microclimate on summertime building cooling demand: a parametric analysis for Antwerp, Belgium, *Appl. Energy* 228 (2018) 852–872, <https://doi.org/10.1016/j.apenergy.2018.06.110>.
- [47] A. Kubilay, J. Allegri, D. Strelbel, Y. Zhao, D. Derome, J. Carmeliet, Advancement in urban climate modelling at local scale: urban heat island mitigation and building cooling demand, *Atmosphere* 11 (2020) 1–20, <https://doi.org/10.3390/atmos11121313>.
- [48] Architectural Institute of Japan, AIJ guideline for practical applications of CFD to pedestrian wind environment around buildings. https://www.aij.or.jp/jpn/publish/cfdguide/index_e.htm, 2020.
- [49] Y. Tominaga, A. Mochida, R. Yoshie, H. Kataoka, T. Nozu, M. Yoshikawa, T. Shirasawa, AIJ guidelines for practical applications of CFD to pedestrian wind environment around buildings, *J. Wind Eng. Ind. Aerod.* 96 (2008) 1749–1761, <https://doi.org/10.1016/J.JWEIA.2008.02.058>.
- [50] Commercial reference buildings | department of energy (n.d.), <https://www.energy.gov/eere/buildings/commercial-reference-buildings>.
- [51] TMY2 weather data | department of energy (n.d.), <https://www.energy.gov/eere/buildings/downloads/tmy2-weather-data>.
- [52] P.A. Mirzaei, J. Carmeliet, Dynamical computational fluid dynamics modeling of the stochastic wind for application of urban studies, *Build. Environ.* 70 (2013) 161–170, <https://doi.org/10.1016/j.buildenv.2013.08.014>.
- [53] J. Franke, A. Hellsten, K.H. Schlünzen, B. Carissimo, The COST 732 Best Practice Guideline for CFD simulation of flows in the urban environment: a summary, *Int. J. Environ. Pollut.* 44 (2011) 419–427, <https://doi.org/10.1504/IJEP.2011.038443>.
- [54] B.E. Launder, B.E. Spalding, D. Brian, *Lectures in Mathematical Models of Turbulence*, Academic Press, Academic Press, New York, 1972.
- [55] T. Galindo, M.A. Hermida, Effects of thermophysiological and non-thermal factors on outdoor thermal perceptions: the Tomebamba Riverbanks case, *Build. Environ.* 138 (2018) 235–249, <https://doi.org/10.1016/j.buildenv.2018.04.024>.
- [56] A. Matzarakis, B. Amelung, Physiological equivalent temperature as indicator for impacts of climate change on thermal comfort of humans, in: *Seasonal Forecasts, Climatic Change and Human Health*, Springer, 2008, pp. 161–172.
- [57] P. Höppe, The physiological equivalent temperature—a universal index for the biometeorological assessment of the thermal environment, *Int. J. Biometeorol.* 43 (1999) 71–75.
- [58] Grasshopper, *GrassHopper 3D Tools*, 2019.
- [59] M. Sadeghipour, *LADYBUG TOOLS*, 2022.
- [60] R. Aghamolaei, M.M. Azizi, B. Aminzadeh, P.A. Mirzaei, A tempo-spatial modelling framework to assess outdoor thermal comfort of complex urban neighbourhoods, *Urban Clim.* 33 (2020), <https://doi.org/10.1016/j.ulclim.2020.100665>.